coatings

MDPI

Article

Structural Features of Cellulose and Cellulose Nanocrystals via In Situ Incorporation of Magnetic Iron Oxide Nanoparticles: Modification and Characterization

Suter Kiplagat Evans [1,*], Omwoyo Nyaigoti Wesley [2], Lawrence Koech [1], Simphiwe Maurice Nelana [2] and Hilary Limo Rutto [1]

[1] Department of Chemical Engineering, Vaal University of Technology, Vanderbijlpark 1911, South Africa
[2] Department of Chemistry, Vaal University of Technology, Vanderbijlpark 1911, South Africa
* Correspondence: esuter78@gmail.com; Tel.: +25-4720048083

Abstract: This work reports on the structural modification of cellulosic materials with magnetic iron oxide nanoparticles through the co-precipitation method. Cellulose is one of the most abundant natural polymers with chemical variability brought about by the presence of several hydroxyl groups, allowing its surface modifications through the insertion of several chemical groups to impact its cellulosic characteristics. Thus, the objective of this study was to synthesize magnetic iron oxide nanoparticles (MNPs) through co-precipitation, followed by in situ incorporation of MNPs onto chemically purified cellulose (CPC) and cellulose nanocrystals (CNC). The composites were characterized for thermal properties using TGA, molecular structure using FTIR, surface morphology using SEM, elemental composition using electron dispersion spectroscopy (EDS), and crystallinity using XRD. The prepared composites presented improved crystal, thermal, and surface properties. CNC-MNPs and CPC-MNPs bore particle sizes of 26.94 and 37.72 nm, respectively, whereas MNPs' particle size was 10.3 nm. EDS analysis indicated that Fe, C, and Cl were the main elements present in the composites. Surface modification of the cellulosic materials presented excellent sorption surface properties and can be used in several industrial processes, such as wastewater purification, air filtration, and various environmental remediation processes.

Keywords: nanotechnology; iron oxide; cellulose; modification; composites; co-precipitation

Citation: Evans, S.K.; Wesley, O.N.; Koech, L.; Nelana, S.M.; Rutto, H.L. Structural Features of Cellulose and Cellulose Nanocrystals via In Situ Incorporation of Magnetic Iron Oxide Nanoparticles: Modification and Characterization. *Coatings* **2023**, *13*, 39. https://doi.org/10.3390/coatings13010039

Academic Editor: Norizah Abdul Rahman

Received: 16 November 2022
Revised: 18 December 2022
Accepted: 20 December 2022
Published: 26 December 2022

1. Introduction

Cellulosic materials have recently attracted a wide range of applications in research, many geared toward environmental engineering. These interests are sought due to the size effects, unique structural properties, and high specific surface areas of cellulosic materials. Additionally, these nanomaterials have attracted much attention from researchers worldwide in industries, medicine, technology, government, and academia [1,2]. Relatively new agro-based nanomaterials have attracted a more significant number of potential applications, which are countless and ever-increasing, and many are already coming to reality [3]. Furthermore, cellulosic materials have a chemical structure that contains numerous hydroxyl groups (OH) which form an interconnected network structure via hydrogen bonding. Due to these hydroxyl groups, cellulose may be easily blended with other materials, such as synthetic and natural polymers and other inorganic materials, to increase mechanical, sorption, electrical, and biological characteristics [4,5].

On the other hand, metal oxide nanoparticles have great importance in medicine and health. The metal and its oxide are more stable at high temperatures and pressures. Magnetic iron oxide nanomaterials are important surface modifiers for cellulosic nanomaterials, especially magnetite (Fe_3O_4) and maghemite (Fe_2O_3). These nanoparticles have gained wide applications in resonance imaging, catalysis, environmental remediation, magnetic fluid, nanocarriers for cancer theragnostic, etc. [6,7]. In addition, magnetic iron

oxide nanoparticles' inertness, biocompatibility, and low toxicity present a magnificent perspective in combination with biotechnology [8].

Modified cellulosic materials are more attractive due to improved features ascribed to their cooperative effects and synergistic properties. The chemical modification process improves covalent bond formation through the interaction between the modifier agent and the interactive center of the solid surface. The insertion of organic molecules into the solid support surface provides superior and additional properties that differ from the original support [9]. Studies on the modifications of cellulosic materials have been developed; these include modification of cellulose with diethylenediamine, aminoethanothiol, carboxymethyl [10], phosphate [11], acryls [12], amine [13], etc. Cellulosic nanomaterials have also been used as organic surface coatings and stabilizers due to their superior properties, such as natural abundance, low cost, renewable, and biodegradability. Cellulosic materials combine with a wide range of nanoparticles to create new bio-nanocomposites with enhanced beneficial properties, such as magnetic, photo-catalytic, electrical conductivity, and antibacterial properties [14].

The bio-composites of magnetic iron oxide cellulose composite are a leading means of producing cheap devices for data storage and security. In addition, modified cellulosic composites have been widely applied as adsorbents in wastewater treatment for the removal of heavy metals and the degradation of organic pollutants.

Various approaches of magnetic iron oxide nanoparticles functionalization onto different materials have been developed. These methods include co-precipitation [15], thermal deposition [16], micro-emulsion [17], the hydrothermal method [18], the polyol medicated method [19], the sol–gel method [20], bio-mineralization [21], and sputter deposition [22]. However, the co-precipitation method has proven the best, giving particle sizes between 5 and 40 nm, with magnetic spin (Ms) of 36.8 $emug^{-1}$, at operating temperatures between 20 and 150 °C, in a synthesis time of 1 h [23,24].

Chira et al. (2019) [25] and Akhtar et al. (2020) [26] used magnetic nanoparticles to study the surface properties and structural features of cellulose nanocrystals. They found that the incorporation of the magnetic nanoparticles strengthened the interactions between the nanocrystals and decreased the crystallinity of the material [25,26]. On the interactions between cellulose nanocrystals and other nanomaterials, the authors found that the incorporation of the magnetic nanoparticles increased the interactions between the materials and improved the stability of the composite material. Similarly, De Oliveira et al. (2019) [27] used magnetic nanoparticles to study the mechanical properties of cellulose nanocrystals. Their findings indicate that the incorporation of the magnetic nanoparticles increased the tensile strength of the material [27]. Conversely, Bharambe et al. (2020) [28] used magnetic nanoparticles to study the nanomechanical properties of cellulose nanomaterials. Their results revealed that the incorporation of magnetic nanoparticles improved the mechanical properties of the material [27,28].

Vilaça et al. (2020) [29] and Duarte et al. (2020) [30] established that the incorporation of magnetic nanoparticles increases the thermal stability of both synthetic and natural polymeric materials [29,30]. Carvalho et al. (2020) [31] and Gomes et al. (2021) [32] used magnetic nanoparticles to study the magnetic properties of cellulose nanocrystals. The authors found that the incorporation of magnetic nanoparticles increased the magnetic response of the material. They further noticed that the electrical properties of cellulose nanomaterials increased with the addition of iron oxide nanoparticles [31,32]. In general, several studies have investigated the structural features of cellulose and cellulose nanocrystals with the incorporation of magnetic iron oxide nanoparticles and compared the properties of the material before and after the incorporation. The results show that the incorporation of magnetic nanoparticles can improve the properties of cellulose nanomaterials, such as the thermal stability, mechanical strength, optical transparency, hydrophilic nature, magnetic response, and electrical conductivity of the material. However, most of the studies did not dwell on comparing the features and behavior of cellulosic material of the same nature

with different particle sizes when incorporated with iron oxide nanoparticles under the same conditions.

In this work, structural modification of the cellulosic materials was performed to improve the crystallinity, particle sizes, thermal stabilities, and surface properties to establish their thermal behavior, crystallinity, and surface properties while drawing comparisons between the two cellulosic materials. The co-precipitation method was chosen for its undebatable features, such as the production of composites with smaller particle sizes, synthesis of an immense amount of nanocomposites within a shorter duration, efficiency, and economical nature in terms of production cost. Additionally, it can be performed without ideal conditions with no complications. The method also enhances the production of a homogenous matrix of the composites.

The study thus was geared toward developing nanocomposites with enhanced properties, such as thermal stability, sorption effectiveness, low cost, environmental friendliness, reusability, and sustainability, for wastewater purification and environmental remediation. This in turn aimed at reducing environmental pollution caused by waste Bagasse disposal; increasing the production of cellulosic materials from waste biomass for industrial, chemical, environmental, and pharmaceutical applications; and producing cellulosic materials that can withstand harsh environmental conditions through modification.

2. Materials and Methods

2.1. Materials

Cellulose nanocrystals and chemically purified cellulose were derived from sugarcane bagasse waste [33]. (The sugarcane bagasse, an agricultural waste, was gathered from the South Nyanza Sugar Company in Awendo, Kenya) (Sony Sugar Company, Nairobi, Kenya). Analytical-grade nitric acid HNO_3 (98.99%), sodium hypochlorite (NaOCl), sulfuric acid H_2SO_4 (99.9%), acetic acid, sodium hydroxide, and acetone (99.9%) were utilized. Deionized water, cerrous sulfate heptahydrate ($FeSO_4 \times 7H_2O$), methanol, iron (III) chloride hexahydrate ($FeCl_3 \times 6H_2O$), and 25% NH_4OH were used throughout the experiments. All the chemicals were purchased from Sigma Aldrich (St. Louis, MO, USA).

2.2. Methods

2.2.1. Synthesis of MNPs through Co-Precipitation

Synthesis of MNPs was conducted as illustrated in Figure 1 below. The process involved measuring 100 mL of deionized water and transferring it to a clean, dry, three-neck round-bottomed flask fitted with a magnetic stirrer and a Liebig condenser. The deionized water in the flask was degassed for 15 min by heating at 80 °C, then bubbled with nitrogen gas for 15 min to establish an inert environment. Next, 3.1 g of ferric chloride hexahydrate and 2.1 g of ferrous sulfate heptahydrate salts were added to the oxygen-free inert water under robust mixing for 1 h. The, 25% NH_4OH was added dropwise into the solution mixture for co-precipitation until the color turned dark brown. The stirring was allowed to continue for 1 h. The residue was allowed to settle and then washed with the deionized water–ethanol mixture in a ratio of 1:1 (20 mL ethanol:20 mL double-deionized water), repeatedly permitting the residue to decant under the influence of a magnet while discarding the supernatant. After that, the pure precipitate obtained was allowed to dry in a vacuum oven for 12 h at 60 °C.

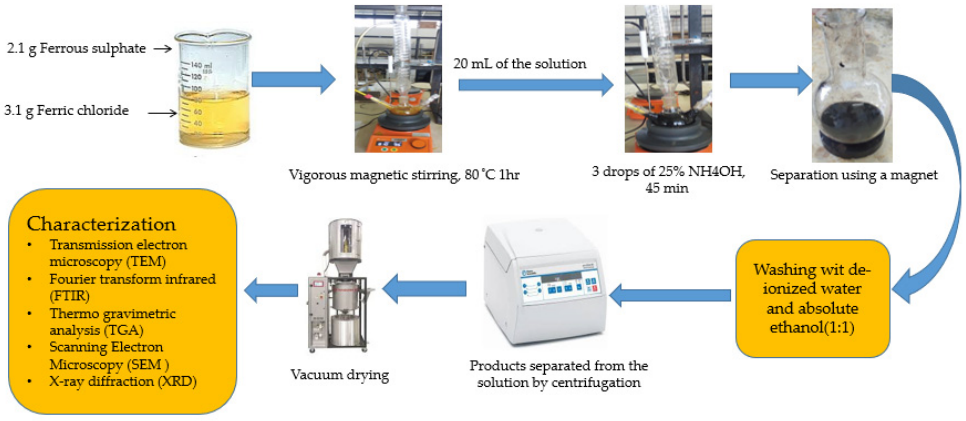

Figure 1. The schematic diagram for the synthesis of MNPs.

2.2.2. Preparation of CPC-MNP Composite through In-Situ Co-Precipitation

Synthesis of MNPs was conducted as illustrated in Figure 2 below. First, 100 mL of deionized water was measured and poured into three-neck round-bottomed flask with 1.5 g CPC powder. The three-neck bottomed flask was equipped with a magnetic stirrer and a Liebig condenser. Degassing of the deionized water in the three-neck flask was conducted for 15 min by heating at 80 °C; then, I was bubbled with nitrogen gas for 15 min to establish an inert environment. Next, 3.1 g of ferric chloride hexahydrate and 2.1 g of ferrous sulfate heptahydrate salts were added into the inert water chemically purified cellulose (WCPC) mixture, under robust mixing for 1 h. Then, 25% NH_4OH was added dropwise into the solution mixture for co-precipitation until the color turned dark brown, after which the stirring process was prolonged for an hour. The residue was allowed to settle and then washed using a deionized water–ethanol mixture, repeatedly permitting the residue to decant under the influence of a magnet and while discarding the supernatant. Finally, the pure residue was dried in a vacuum oven for 12 h at 60 °C.

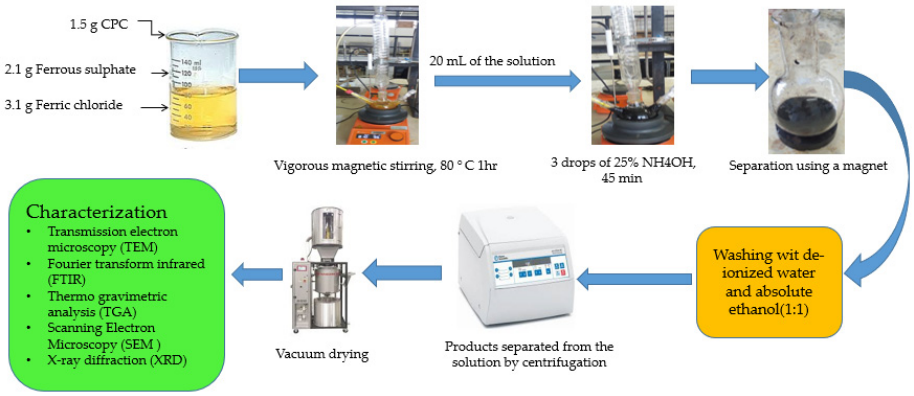

Figure 2. The schematic diagram for the synthesis of CPC-MNPs.

For the preparation of CNC-MNP nanocomposites, the above procedure was repeated; in the place of chemically purified cellulose, cellulose nanocrystals were used.

2.3. Characterization

2.3.1. Fourier Transform Infrared Spectroscopy (FTIR)

Nicolet, iS50, FT-IR (Thermo Nicolet, Thermo Fisher Scientific, Madison, WI, USA) infrared spectroscopy was used to determine the molecular structures of the MNPs and the produced composites (MNPs, CPC-MNPs, and CNC-MNPs). In the transmittance mode, the spectra of the magnetic nanoparticles and the produced composites were recorded in the range of 4000 to 500 cm^{-1}. The baseline was estimated by initially running the background before placing the sample on the sample holder and obtaining the scans in the

range of 500 and 4000 cm^{-1}. The spectra were normalized at 1230 cm^{-1} and corrected by the baseline. Finally, the peaks from the library were identified and matched to the chemical structures. All samples were analyzed in triplicate to validate the obtained spectra.

2.3.2. Thermal Properties

A Perkin Elmer Pyris 1 Thermogravimetric analyzer (TGA) was used to quantify the loss of mass for the materials under a controlled temperature change. Approximately 11.000 mg of MNPs, CPC-MNPs, and CNC-MNPs were examined using a TGA (Pyris 1; Perkin Elmer, MA, USA) Thermogravimetric analyzer linked to an inert nitrogen gas flow and heated at a rate of 10 °C/min from 30 to 1000 °C. TGA was also utilized to validate the approximate percentage weight loss with temperature change and the successful loading capacities of MNPs on CPC-MNP and CNC-MNP composites.

2.3.3. Morphological Properties

Field emission Scanning electron microscopy (FE-SEM, JEOL-JSM, JEOL Ltd, Tokyo, Japan) was used to directly investigate the surface characteristics and to observe the produced composites' morphological appearance. The photographs were taken at an operating voltage of 5 kV. Before the SEM measurements, the samples were coated with a 7 nm thick gold under a high vacuum environment.

2.3.4. Crystal Properties

A Shimadzu XRD-700 X-ray diffractometer (Shimadzu Corporation, Kyoto, Japan) with a scanning rate of 10 °C per min, and Cu Kα radiation source (λ = 1.54060 Å) operating at 40 kV and 30 mA was used to investigate the crystal characteristics of the produced composites with MNPs. The XRD patterns were recorded across a 2θ = 10–80° angular range. The Scherrer equation was used to calculate the crystal size in (nm).

$$\text{Crystal size (D)} = \frac{K\lambda}{\beta\, Cos\, \theta} \tag{1}$$

where D is the crystal size of the particle (nm), K is Scherrer constant (K = 0.91), the X-ray wavelength (1.54060 Å) was given by λ, β is full width at half maximum (FWHM) of the diffraction peak, and θ is the angle of diffraction.

The crystallinity index (C_rI) is an important parameter for understanding the structural features of compounds. The C_rI values of the MNPs and the composites were calculated using Equation (2) below.

$$C_rI(\%) = \frac{I_{002} - I_{am}}{I_{002}} \times 100 \tag{2}$$

where I_{002} is the maximum intensity of the 002 lattice diffraction peak and I_{am} is the intensity scattered by the amorphous part of the sample.

2.3.5. Elemental Determination

Electron diffraction spectrum (EDS) EOL JEM 2100 LaB6, JEOL Ltd., Tokyo, Japan) analysis was carried out to quantify the contents of various elements present in the prepared composites.

2.3.6. Particle Size Analysis

The images of MNPs, CPC-MNPs, and CNC-MNPs were captured using at transmission electron microscope (Tecnai G2 20 S-twin, FEI Company, Hillsboro, OR, USA). The samples were dispersed in an appropriate aqueous solution, and then a thin carbon film (0.1 wt.%) was placed on the surface of a copper grid covered with thin carbon film. Thereafter, the samples were dried before conducting TEM analysis at an accelerating voltage of 100–120 kV.

2.4. Data Analysis

Origin Pro 2018 statistical software (version 9.5.1) was used to draw the FTIR (Fourier transform infrared) spectra, XRD graphs, TGA (thermogravimetric analysis) curves, and DTG (derivative thermogravimetric) curves from the raw data obtained during characterization.

3. Results and Discussion

3.1. XRD Patterns for MNPs, CPC-MNPs, and CNC-MNPs

Figure 3 shows the XRD patterns for MNPs, CPC-MNPs, and CNC-MNPs. Both MNPs and nanocomposites displayed spectral peaks at 2θ ≈ 30.27°, 35.86°, 43.82°, 54.19°, 57.5°, and 63.2°, which corresponded to indices (220), (311), (400), (422), (511), and (440), respectively. These spectral peaks corresponded and tallied with data for synthetic magnetite according to the JCPDS 019-0629 and JCPDS 039-1346 [34,35]. The amorphous peak for synthesized cellulose was also at 2θ ≈ 22.4° for CPC-MNPS. This peak is not seen in CNC-MNPs spectra, indicating that cellulose nanocrystals displayed higher crystallinity than chemically purified cellulose (Appendix A) [33].

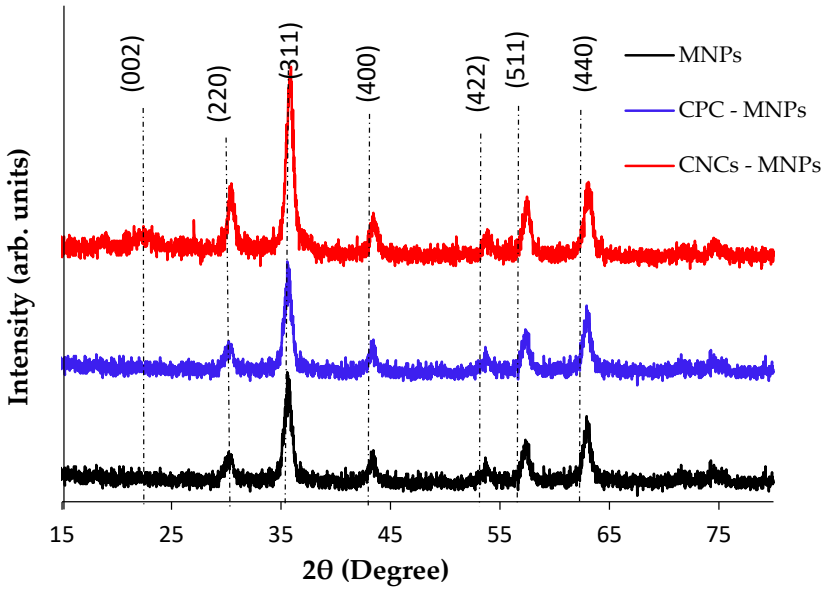

Figure 3. XRD patterns for MNPs, CPC-MNPs, and CNC-MNPs.

The crystallinity of composites is significant in determining thermal stability, elasticity, sorption efficiency, and other physical properties vital in industrial applications. Increased crystallinity enhances the substance's rigidity and stiffness, hence boosting its strength. As a result, compounds with improved mechanical characteristics can be created [36]. The in situ incorporation of MNPs onto CPC and CNC improved the crystallinity, as observed in the diffraction patterns (Figure 3). This can also be confirmed by the C_rI values in Table 1, where there are considerably higher crystallinity values of 88.68% for MNPs, 81.78% for CNC-MNPs, and 72.25% for CPC-MNPs. When compared to the precursors (Appendix A) [33], the integration of MNPs enhanced the crystallinity of the cellulosic materials.

Table 1. Crystallinity Indices for MNPs, CPC-MNPS, and CNC-MNPs.

Sample	$2\theta_{(Amorphous)}$ (°)		$2\theta_{(002)}$ (°)		Crystallinity Index (CrI %)
	Degree	Intensity, I_{am}	Degree	Intensity, I_{002}	
MNPs	22.42	55.87	36.16	493.43	88.68
CPC-MNPs	22.40	87.53	35.94	339.88	72.25
CNC-MNPs	22.49	69.54	35.7	382.23	81.81

The results further established reduced particle size for the prepared composites, and this was more pronounced in the CNC-MNPs composite in comparison to CPC-MNPs. According to the calculated data obtained using the Scherrer equation, CNC-MNP and CPC-MNP composites had particle sizes of 24.12 nm and 32.8 nm respectively, while MNP had a particle size of 10.3 nm.

Several studies established that the crystallinity of composites can be further improved when nanoparticles are incorporated into cellulosic materials. Li et al. (2020) [37] showed that the incorporation of graphene oxide into cellulose nanocrystals led to an increase in the crystallinity index from 77.16% to 87.12%. Similarly, Li et al. (2019) [38] found that the crystallinity of cellulose-nanocrystal-reinforced bio-nanocomposites rose from 78.24% to 92.15% when silica nanoparticles were incorporated [37,38].

Marques et al. (2020) used X-ray diffraction (XRD) to investigate the structures of cellulose nanocrystals (CNC) and CNC-magnetic iron oxide nanoparticles (MNPs) [39]. The results indicated that the CNC-MNPs had higher crystallinity than the CNC alone, suggesting that the MNPs had a stabilizing effect on the crystalline structure of the CNC. In addition, Gül et al. (2018) [40] used XRD to investigate the effects of doping with iron oxide nanoparticles on the crystallinity, mechanical properties, and thermal stability of cellulose nanocomposites [40]. The results showed that the CNC-MNPs had improved crystallinity, mechanical properties, and thermal stability compared to the CNC alone. In general, the incorporation of MNPs into natural polymers can improve the structural, mechanical, optical, and thermal properties of their nanocomposites [40].

3.2. Molecular Structures of the MNPs, CPC-MNPs, and CNC-MNPs Nanocomposites

The IR spectra of magnetic nanoparticles (MNPs), modified cellulosic materials (CPC-MNPs), and CNC-MNP nanocomposites are presented in Figure 4a. The spectra of cellulosic materials (CPC and CNC) were obtained from our previous work; see Figure 4b [33]. There were slight variations in the positions and intensity of the functional group signals of the nanocomposites after the in situ incorporation of MNPs. At around 3340 cm^{-1}, the flattened peak, which is associated with O-H stretching of intramolecular hydrogen bonds of the CPC and CNC from Figure 4b, is observed to decrease in intensity as a result of Fe attaching itself to O-H groups present on the surfaces of the chemically purified cellulose, which associates with a reduction in hydroxyl groups' intensity [41]. This effect is more pronounced for the CNC-MNP nanocomposite in comparison to the CPC-MNP nanocomposite. The modest shifts in the peaks of CPC-MNPs and CNC-MNPS nanocomposites at about 1261 to 1226 cm^{-1} in the identical IR spectra are due to the production of carboxylic acids and aldehyde groups in the process of in situ integration of MNPs [42]. Peaks between 1649 and 1634 cm^{-1} of MNPs, CPC-MNPs, and CNC-MNPs were caused by O-H bending caused by adsorbed water [43].

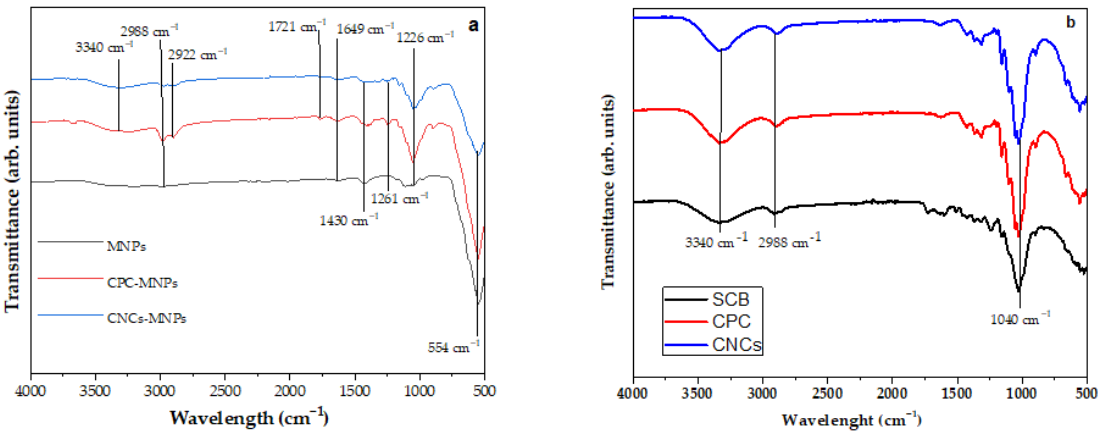

Figure 4. FTIR spectra: (**a**) MNPs, CPC-MNPs, and CNC-MNPs; (**b**) SCB, CPC, and CNC.

Peaks between 1430 and 1420 cm^{-1} in the identical spectra of CPC-MNPs and CNC-MNPs are due to the CH_2 scissoring motion in cellulose. Additionally, the spectral peaks between 1727 to 1721 cm^{-1} of both cellulosic materials composites shifted to 1226 and 1601 cm^{-1}. After the structural modification of the cellulosic materials, the peaks around 2988 and 2292 cm^{-1}, which are associated with the C-H stretching of the cellulosic materials, persisted, though with slight reductions in intensity. This observation indicated that the structural properties of the cellulosic materials were not completely altered. Additionally, the presence of the peaks at 2922 and 554 cm^{-1} of the prepared nanocomposites confirmed successful incorporation.

3.3. Thermal Properties

The experimental research of thermal properties of materials (TGA-DTG) is a dynamic phenomenological technique for studying the response to temperature change. Thermal-gravimetric curves reveal weight changes during heating, whereas their derivation indicates changes in the TGA slope which may not be easily observed. The thermal characteristics of the produced MNPs and cellulosic composites were investigated to determine their thermal stabilities (Figure 5a). The TGA results confirmed that MNPs were stable. There is no observable mass change throughout the degradation curve from 30 to 600 °C. Additionally, in Figure 5a, multi-step degradation for CPC-MNPs and CNC-MNPs is seen at temperatures below 150 °C, resulting from the loss of moisture absorbed by the composites [44].

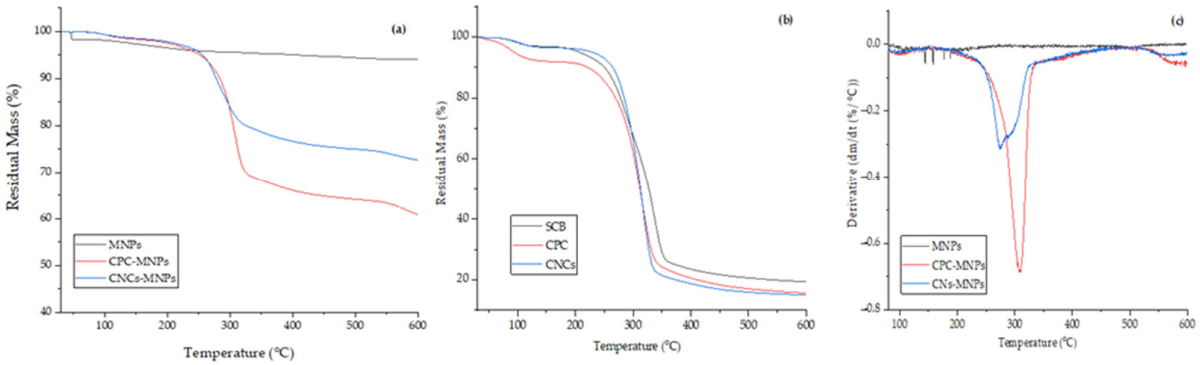

Figure 5. TGA curves for (**a**) MNPs, CPC-MNPs, and CNC-MNPs; (**b**) SCB, CPC, and CNC. DTG curves for (**c**) MNPs, CPC-MNPs, and CNC-MNPs.

Furthermore, the weight loss in the composites preceded the moisture loss. The weight loss between 150 and 230 °C was a result of the hemicelluloses that were not eliminated in the preparation and synthesis of both the CPC and CNC (Figure 5b) [45]. The weight loss was more pronounced in CPC-MNPs in comparison to CNC-MNPs, indicating that CPC-MNPs had much lignin and hemicellulose. According to a similar study, Candido et al. [45] found that, at about 230–460 °C, the weight loss resulted from lignin that was not eliminated. For the MNPs, the slow weight loss between 220 and 330 °C resulted from the dihydroxylation of Fe_3O_4 to FeO [35]. Moreover, the weight loss of the nanocomposites from 310 to 470 °C was due to the reduction of Fe_2O_3 to Fe_3O_4, with the release of CO [46]. Above 480 °C, there was an increase in the weight of the MNPs; this is attributed to the oxidation of magnetite at higher temperatures. The final decomposition of the composites between 480–600 °C involved weight loss of the solid residue—slight weight loss of between 10–12%. The absolute weight loss of the MNPs was less than 5%, whereas for CNC-MNPs it was 16%. CPC-MNPs had the largest absolute weight loss of approximately 20% [47]. The reduced thermal stability of CNC-MNPs resulted from remnant sulfate ions used in the hydrolysis of CPC. This is because the elimination of sulfated anhydrous-glucose units requires lower temperatures [48]. The composition of the magnetic iron oxide nanoparticles in the cellulosic composites was calculated using Equation (2). LTotal and LMNPs are total iron oxide and iron oxide nanoparticles' weight loss [49]. The composition of MNPs in the cellulosic composites was found to be (36.70 ± 0.01) wt.% for CPC-MNPs and (40.45 ± 0.03)

wt.% CNC-MNPs, respectively. Given Figure 5a, incorporating MNPs into the CPC and CNC improved their thermal stabilities (Figure 5b) [33].

$$\text{MNPs wt\%} = \frac{1 - \text{LTotal}}{1 - \text{LMNPs}} \times 100\% \quad (3)$$

The DTG curves (Figure 5c) indicate degradation of CPC-MNPs and CNC-MNPs in three stages of pyrolysis; first, at 220–270 °C, followed by degradation at 270–330 °C, and finally at 330–470 °C. The mechanism involves two pyrolysis processes that are well separated. The DTG curves' temperature peaks occurred at much lower temperatures than for the native cellulose [50]. From the thermal analysis, char formation from CNC-MNPs was the most, at 3.83 wt.%. CPC-MNPs produced 2.62 wt.%. CPCs-MNPs consist of crystalline and amorphous domains, in addition to the low-temperature-degraded materials composed of lignin, hemicellulose, and pectin [51]. The highest char content for the CNC-MNP composite stemmed from the highly crystalline nature of CNC precursors that are attributed to the increased proportion of carbon associated with the increased char [51]. As a result, H_2SO_4, used during the hydrolysis process, acting as a dehydrating agent, facilitated the depolymerization of cellulose by removing some of the –OH groups [52]. The most char being produced by CNC-MNPs is articulated to be a result of its nano-size and the more significant number of free ends of its chains that degrade at lower temperatures.

The TGA and DTG data were used to calculate the heat released and the enthalpy change during the combustion of the MNPs and the composites. The heat released by the composites was calculated by determining the energy released during the heating process. The findings are presented in Table 2 below.

Table 2. Heat released and ΔH of MNPs and the composites.

Material	Onset Temperature (°C)	Maximum Peak Temperature (°C)	Heat Release (J)	ΔH (J/mol)
MNPs	30	-	-	-
CPC-MNPs	30	274.56	1.69	13.63
CNC-MNPs	30	308.58	1.54	13.92

The onset temperatures for MNPs, CPC-MNPs, and CNC-MNPs were relatively similar; however, the maximum peak temperature for CNC-MNPs was significantly higher than that of CPC-MNPs, indicating that the CPC-MNPs had lower thermal resistance. This is likely because CPC-MNPs are more amorphous than other CNC. Additionally, the heat release of CPC-MNPs was much higher than that of CNC-MNPs, likely due to CPC-MNPs having weaker thermal resistance, meaning that more energy is needed to induce a reaction. The enthalpy change for CPC-MNPs was also smaller than that for CNC-MNPs, indicating that less energy is required to induce a reaction in CPC-MNPs than in CNC-MNPs. This is attributed to an additional barrier provided by CNC, preventing the reaction from occurring [53].

These findings could suggest that the incorporation of iron oxide nanoparticles increased the thermal stability of the cellulose and cellulose nanocrystals, but with a slight difference. Furthermore, the findings revealed that the addition of iron oxide nanoparticles could have led to the formation of a protective layer around cellulose and cellulose nanocrystals, which further increased their thermal stability. The protective layer is perceived to create a buffer between the cellulose and cellulose nanocrystals and the external environment, which prevents the decomposition of the material and thus increases its thermal stability [53,54].

3.4. Morphological Studies

Figure 6 shows SEM images of the composites under the same magnification. The micrograph shows white and black surfaces uniformly distributed on the composite surface,

which indicates that the CNC and the iron oxide nanoparticles were well dispersed on the composite. Additionally, the surface was coarse due to visible pores, and it was a homogeneous matrix with a large surface area. The particle sizes of the composites were small. There were few agglomerations (Figure 6a).

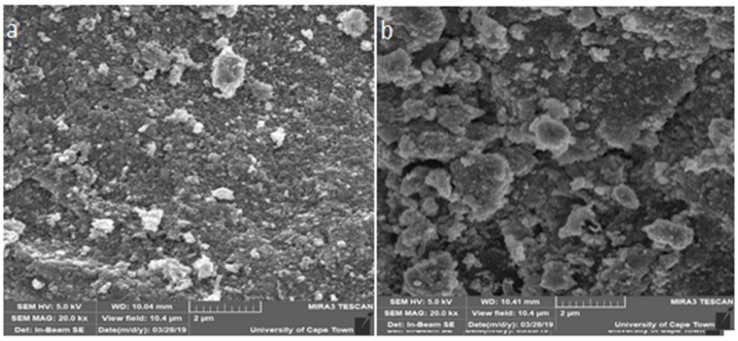

Figure 6. SEM images for CNC-MNPs (**a**) and CPC-MNPs (**b**).

Figure 6b displays dark grey and light grey surfaces of the CPC-MNPs that are well distributed on the surface of the composite. The CPC-MNPs composites were dominated by agglomerates containing fewer pores on their surfaces. The agglomerations are considered to be a result of the amorphous nature of the CPC precursor, which resulted from amorphous cellulose II. From the micrographs, we can see that in situ incorporation of MNPs onto the cellulosic materials enhances the preparation of a homogeneous composite with well-dispersed particle sizes. However, composites prepared from CPC displayed several agglomerations, a poor property of composites. In contrast, the nano-range CNC provide more binding sites of the MNPs, resulting in the production of composites with better surface properties.

3.5. Particle Size Determination

Transmission electron microscopy was used to confirm morphological information obtained from the SEM data and particle sizes obtained from XRD. ImageJ (ij-153) software was used to measure the diameters and circumferences of the particles. Figure 7a–c illustrates micrographs from the TEM characterization of MNPs and the mean particle size of the produced composites. Figure 7(a1) shows a TEM image with a magnification of 200 nm. The image is predominantly composed of small nanoclusters that were agglomerated and measured between 4 and 17 nm in size and had an average diameter of 11.22 nm, as shown in the histogram Figure 7(a2). These data were compared with XRD particle sizes of 10.30 nm calculated using the Scherrer equation (Section 3.1).

Figure 7(b1) shows the CPC-MNPs image with the same magnification (200 nm). The micro-image shows that the composite particles were spherical but not uniform in size. Some of the particles had uneven shapes with several agglomerations at the center and slightly scattered toward the edges of the micrographs. The particle diameters ranged between 10 and 70 nm; the average diameter was 37.72 nm, as indicated by histogram Figure 7(b2). The results for CNC-MNPs showed that the particle sizes ranged from 10 to 50 nm; the average diameter was 26.94 nm. See Figure 7(c1,c2). The composite micrograph shows somehow spherical particles, non-uniform in size, with a lot of agglomerations.

The results from this study are comparable with other research on the synthesis and modification of iron oxide nanoparticles. For instance, Krishnamurthy et al. [55] reported that iron oxide nanoparticles have an average size of 13.50 nm when synthesized by the hydrothermal method. Additionally, Zhou et al. reported that the average size of iron oxide nanoparticles synthesized by the chemical precipitation method was 9.10 nm [56]. These results are comparable to the particle size of MNPs obtained in this study, which was 11.22 nm. Regarding the particle size of the modified cellulosic materials, the results of this study are in agreement with research by Liu et al., who reported that the particle size of CPC-MNPs is between 20 and 90 nm, which is consistent with the results obtained in this

study [57]. Similarly, Zhang et al. reported that the particle size of CNC-MNPs is between 6 and 80 nm, which is also consistent with the results of this study [58]. It can be noted that the results of this study are consistent with other research work regarding the particle sizes of iron oxide nanoparticles and modified cellulosic materials [55].

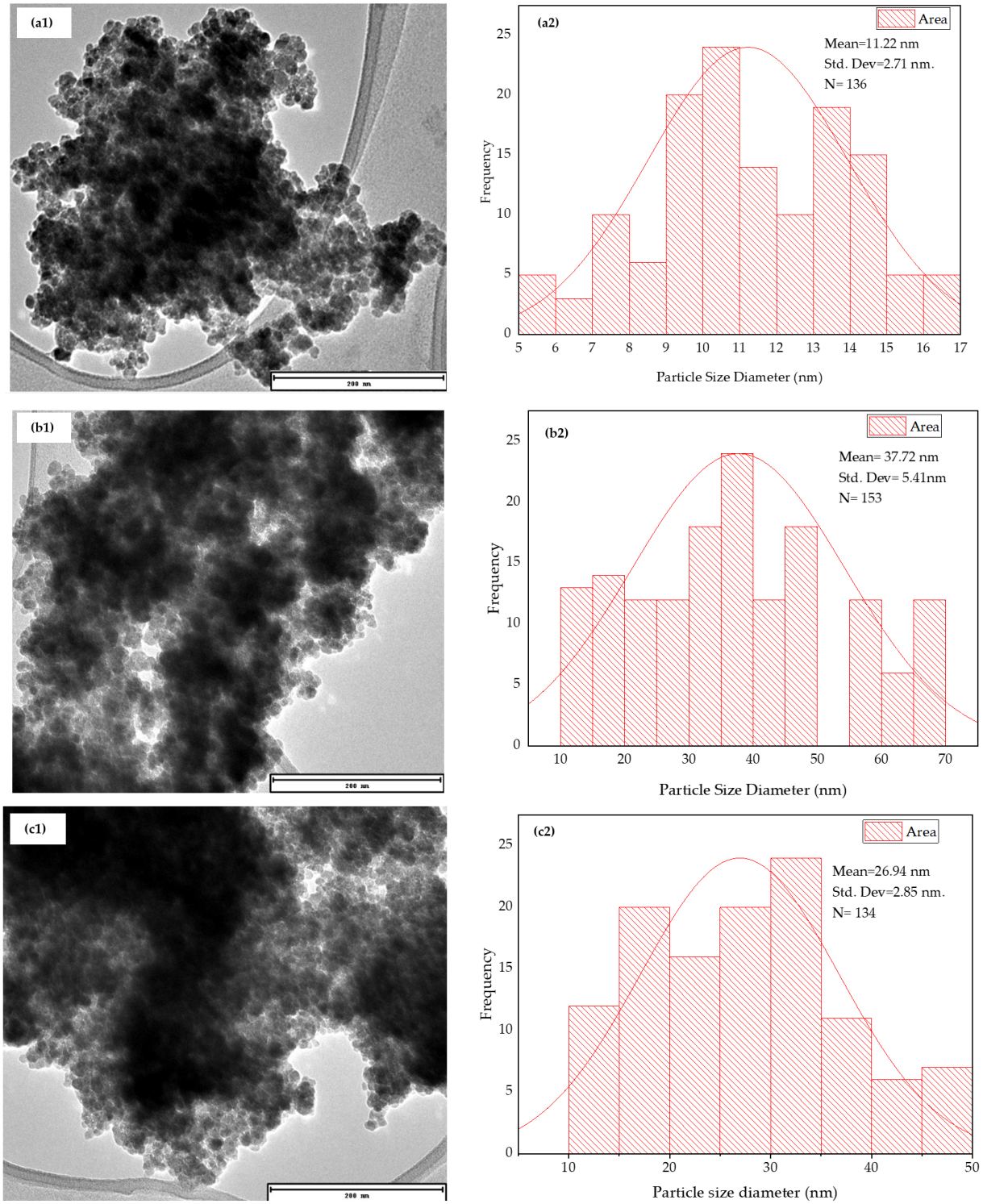

Figure 7. TEM micrographs and histogram for MNPs (**a1**,**a2**), CPC-MNPs (**b1**,**b2**), and CNC-MNPs (**c1**,**c2**).

3.6. Elemental Analysis

Energy dispersive X-ray diffraction spectroscopy (EDS) was carried out to quantify the elemental composition of the prepared composites (Figure 8).

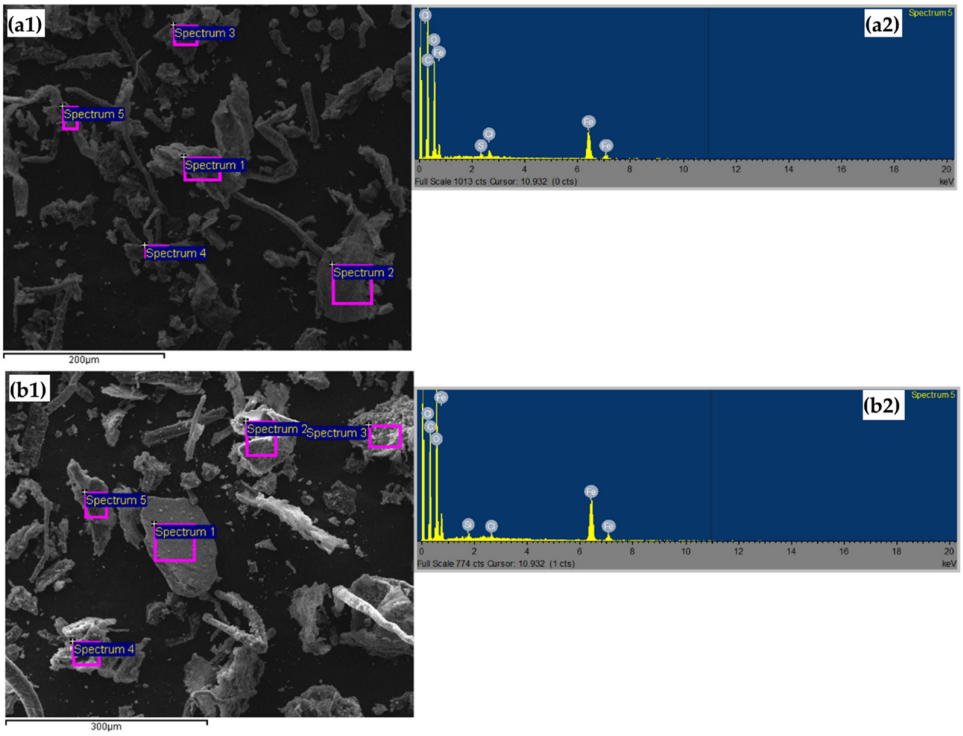

Figure 8. EDS micrographs and spectra for CNC-MNPs (**a1**,**a2**) and CPC-MNPs (**b1**,**b2**).

The EDS for CPC-MNPs displays the peaks of Fe, C, O, Cl, S, and Si (Figure 8(a2)), whereas CNC-MNPs have Fe, C, O, Cl, and S peaks (Figure 8(b2)). All the elements present in the composites corresponded to their appropriate binding energies, Kev. The elements Cl, S, and Fe were presumed to emanate from FeCl and $FeSO_4$ used during the in situ synthesis of the composites. C and O emanated from CNC and CPC precursors. From CNC-MNPs spectra, Si is a result of impurities from the sample collection site of sugarcane bagasse, which was the primary precursor in the synthesis of chemically purified cellulose [33]. The silica disappeared during the acid hydrolysis of CPC to form cellulose nanocrystals. In situ incorporation of the MNPs onto the cellulosic materials indicates that the composites were successfully prepared, and iron oxide nanoparticles were incorporated into CNC and CPC.

4. Conclusions

The in situ integration of MNPs into cellulosic composites during co-precipitation modification resulted in a material with enhanced structural and physical characteristics. From the FTIR analysis, the presence of the peaks at around 2922 cm^{-1} associated with cellulosic materials and 554 cm^{-1} associated with MNPs indicated successful preparation of the cellulosic composites. The XRD data also proved that the prepared composites' particle size and crystal properties were improved. From the scanning electron microscopy, the CNC-MNP composite presented a homogeneous surface with fewer agglomerations than CPC-MNPs, which displayed several agglomerations with clumps on its surface. The EDS spectrum indicated that Fe, C, O, and Cl were the main elements. Si and S were present in small percentages. All elements corresponded to their binding energies, Kev. This study confirmed that the CNC-MNPs and CPC-MNPs composites have excellent features when compared to the precursor materials.

Author Contributions: Conceptualization, S.K.E.; data curation, L.K.; formal analysis, O.N.W.; Investigation, S.K.E.; methodology, S.K.E.; project administration, S.K.E. and O.N.W.; resources, O.N.W. and S.M.N.; software, L.K.; Supervision, O.N.W. and H.L.R.; validation, L.K.; visualization, L.K.; writing—original draft, S.K.E.; writing—review and editing, O.N.W., H.L.R., S.M.N. and L.K. All authors have read and agreed to the published version of the manuscript.

Funding: This research received no external funding.

Institutional Review Board Statement: Not applicable.

Informed Consent Statement: Not applicable.

Data Availability Statement: The data presented in this study are openly available in Heliyon at http://dx.doi.org/10.1016/j.heliyon.2019.e02635. All experimental data are available within this research article.

Acknowledgments: The authors wish to acknowledge the Department of Chemical Engineering and Chemistry, the Vaal University of Technology, for the provision of necessary laboratory space, chemicals, and equipment for the success of the work.

Conflicts of Interest: The authors declare no conflict of interest.

Appendix A

Table A1. Crystallinity of SCB, CPC, and CNC.

Sample	$2\theta_{(Amorphous)}$ (°)		$2\theta_{(002)}$ (°)		Crystallinity Index (CrI %)
	Degree	Intensity, I_{am}	Degree	Intensity, I_{002}	
SCB	16.34	394	22.28	664	40.66
CPC	16.12	292	22.38	892	67.26
CNC	16.32	214	22.34	926	76.89

References

1. Gopinath, K.P.; Rajagopal, M.; Krishnan, A.; Sreerama, S.K. A Review on Recent Trends in Nanomaterials and Nanocomposites for Environmental Applications. *Curr. Anal. Chem.* **2021**, *17*, 202–243. [CrossRef]
2. Chen, Z.; He, X.; Ge, J.; Fan, G.; Zhang, L.; Parvez, A.M.; Wang, G. Controllable fabrication of nanofibrillated cellulose supported HKUST-1 hierarchically porous membranes for highly efficient removal of formaldehyde in air. *Ind. Crop. Prod.* **2022**, *186*, 115269. [CrossRef]
3. Dubey, S.K.; Pandey, A.; Sangwan, R.S. *Current Developments in Biotechnology and Bioengineering: Crop Modification, Nutrition, and Food Production*; Elsevier: Amsterdam, The Netherlands, 2016; ISBN 0444636722. [CrossRef]
4. Mansoori, S.; Davarnejad, R.; Matsuura, T.; Ismail, A.F. Membranes based on non-synthetic (natural) polymers for wastewater treatment. *Polym. Test.* **2020**, *84*, 106381. [CrossRef]
5. Karapanagioti, H.K.; Werner, D. Sorption of hydrophobic organic compounds to plastics in the marine environment: Sorption and desorption kinetics. *Hazard. Chem. Assoc. Plast. Mar. Environ.* **2018**, *78*, 205–219. [CrossRef]
6. Aragaw, T.A.; Bogale, F.M.; Aragaw, B.A. Iron-based nanoparticles in wastewater treatment: A review on synthesis methods, applications, and removal mechanisms. *J. Saudi Chem. Soc.* **2021**, *25*, 101280. [CrossRef]
7. Barani, M.; Rahdar, A.; Mukhtar, M.; Razzaq, S.; Qindeel, M.; Olam, S.A.H.; Paiva-Santos, A.C.; Ajalli, N.; Sargazi, S.; Balakrishnan, D.; et al. Recent application of cobalt ferrite nanoparticles as a theranostic agent. *Mater. Today Chem.* **2022**, *26*, 101131. [CrossRef]
8. Zhu, H.; Jiang, S.; Chen, H.; Roco, M.C. International perspective on nanotechnology papers, patents, and NSF awards (2000–2016). *J. Nanopart. Res.* **2017**, *19*, 370. [CrossRef]
9. Bordet, A.; Leitner, W. Metal Nanoparticles Immobilized on Molecularly Modified Surfaces: Versatile Catalytic Systems for Controlled Hydrogenation and Hydrogenolysis. *Acc. Chem. Res.* **2021**, *54*, 2144–2157. [CrossRef]
10. Bezerra, R.D.S.; Leal, R.C.; da Silva, M.S.; Morais, A.I.S.; Marques, T.H.C.; Osajima, J.A.; Meneguin, A.B.; Barud, H.D.S.; da Silva Filho, E.C. Direct Modification of Microcrystalline Cellulose with Ethylenediamine for Use as Adsorbent for Removal Amitriptyline Drug from Environment. *Molecules* **2017**, *22*, 2039. [CrossRef]
11. Luneva, N.K.; Petrovskaya, L.I.; Ezovitova, T.I. Synthesis and properties of cellulose phosphates. *Russ. J. Appl. Chem.* **2007**, *80*, 1923–1927. [CrossRef]

12. Safavi-Mirmahalleh, S.-A.; Salami-Kalajahi, M.; Roghani-Mamaqani, H. Effect of surface chemistry and content of nanocrystalline cellulose on removal of methylene blue from wastewater by poly(acrylic acid)/nanocrystalline cellulose nanocomposite hydrogels. *Cellulose* **2019**, *26*, 5603–5619. [CrossRef]
13. Koga, H.; Kitaoka, T.; Isogai, A. In situ modification of cellulose paper with amino groups for catalytic applications. *J. Mater. Chem.* **2011**, *21*, 9356–9361. [CrossRef]
14. Umavathi, S.; Ramya, M.; Padmapriya, C.; Gopinath, K. Green Synthesis of Zinc Oxide Nanoparticle Using *Justicia procumbense* Leaf Extract and Their Application as an Antimicrobial Agent. *J. Biol. Act. Prod. Nat.* **2020**, *10*, 153–164. [CrossRef]
15. Biehl, P.; von der Lühe, M.; Dutz, S.; Schacher, F.H. Synthesis, Characterization, and Applications of Magnetic Nanoparticles Featuring Polyzwitterionic Coatings. *Polymers* **2018**, *10*, 91. [CrossRef]
16. Effenberger, F.B.; Couto, R.A.; Kiyohara, P.K.; Machado, G.; Masunaga, S.H.; Jardim, R.F.; Rossi, L.M. Economically attractive route for the preparation of high-quality magnetic nanoparticles by the thermal decomposition of iron (III) acetylacetonate. *Nanotechnology* **2017**, *28*, 115603. [CrossRef]
17. Yousuf, M.A.; Jabeen, S.; Shahi, M.N.; Khan, M.A.; Shakir, I.; Warsi, M.F. Magnetic and electrical properties of yttrium substituted manganese ferrite nanoparticles prepared via micro-emulsion route. *Results Phys.* **2020**, *16*, 102973. [CrossRef]
18. Torres-Gómez, N.; Nava, O.; Argueta-Figueroa, L.; García-Contreras, R.; Baeza-Barrera, A.; Vilchis-Nestor, A.R. Shape Tuning of Magnetite Nanoparticles Obtained by Hydrothermal Synthesis: Effect of Temperature. *J. Nanomater.* **2019**, *2019*, 7921273. [CrossRef]
19. Majidi, S.; Sehrig, F.Z.; Farkhani, S.M.; Goloujeh, M.S.; Akbarzadeh, A. Current methods for synthesis of magnetic nanoparticles. *Artif. Cells Nanomed. Biotechnol.* **2016**, *44*, 722–734. [CrossRef]
20. Kayani, Z.N.; Arshad, S.; Riaz, S.; Naseem, S. Synthesis of Iron Oxide Nanoparticles by Sol–Gel Technique and Their Characterization. *IEEE Trans. Magn.* **2014**, *50*, 2200404. [CrossRef]
21. Tampieri, A.; Sprio, S.; Sandri, M.; Valentini, F. Mimicking natural bio-mineralization processes: A new tool for osteochondral scaffold development. *Trends Biotechnol.* **2011**, *29*, 526–535. [CrossRef]
22. Hemben, A.; Chianella, I.; Leighton, G. Surface Engineered Iron Oxide Nanoparticles Generated by Inert Gas Condensation for Biomedical Applications. *Bioengineering* **2021**, *8*, 38. [CrossRef] [PubMed]
23. Gruskiene, R.; Krivorotova, T.; Staneviciene, R.; Ratautas, D.; Serviene, E.; Sereikaite, J. Preparation and characterization of iron oxide magnetic nanoparticles functionalized by nisin. *Coll. Surf. B Biointerfaces* **2018**, *169*, 126–134. [CrossRef] [PubMed]
24. Dhalani, J.; Kapadiya, K.; Pandya, M.; Dubal, G.; Imbraj, P.; Nariya, P. Magnetic Nanoparticles: Synthesis, Protection, Functionalization, and Application. *Angew. Chem. Int. Ed.* **2018**, *46*, 1222–1244. [CrossRef]
25. Chira, S.C.; Kocabas, C.; Mathew, A.P. Modification of cellulose nanocrystals using magnetic iron oxide nanoparticles for enhanced properties. *Green Process. Synth.* **2019**, *8*, 545–552.
26. Akhtar, M.; Hanif, M.; Khalid, M. Modification of cellulose nanocrystals using magnetic iron oxide nanoparticles. *Mater. Res. Express* **2020**, *7*, 045012.
27. De Oliveira, R.M.; Souza, V.M.; Tenório, A.C.; Carvalho, A.M. Cellulose nanocrystals reinforced with magnetic iron oxide nanoparticles: A mechanical and morphological study. *Polymers* **2019**, *11*, 48.
28. Baldikova, E.; Pospiskova, K.; Ladakis, D.; Kookos, I.K.; Koutinas, A.A.; Safarikova, M.; Safarik, I. Magnetically modified bacterial cellulose: A promising carrier for immobilization of affinity ligands, enzymes, and cells. *Mater. Sci. Eng.* **2017**, *71*, 214–221. [CrossRef]
29. Vilaça, P.B.; de Sousa, M.C.F. Effect of magnetic nanoparticles on the thermal behavior of cellulose nanofibrils. *Mater. Chem. Phys.* **2020**, *241*, 122522.
30. Duarte, L.F.; Caetano, R.C.; dos Santos, I.L. Magnetic nanoparticles-cellulose nanocrystals nanocomposites: Thermal, mechanical and morphological properties. *Mater. Chem. Phys.* **2020**, *247*, 122938.
31. Carvalho, S.G.; Oliveira, R.M.; Lanza, M.R.V.; Carvalho, A.M. Magnetic cellulose nanocrystals: Impact of iron oxide nanoparticles on magnetic response. *Mater. Chem. Phys.* **2020**, *245*, 122866.
32. Gomes, J.T.; de Oliveira, R.M.; Tenório, A.C.; Carvalho, A.M. Magnetic cellulose nanocrystals: Impact of iron oxide nanoparticles on electrical properties. *Mater. Chem. Phys.* **2021**, *260*, 123675.
33. Evans, S.K.; Wesley, O.N.; Nathan, O.; Moloto, M.J. Chemically purified cellulose and its nanocrystals from sugarcane bagasse: Isolation and characterization. *Heliyon* **2019**, *5*, 02635. [CrossRef]
34. Ansari, S.A.M.K.; Ficiarà, E.; Ruffinatti, F.A.; Stura, I.; Argenziano, M.; Abollino, O.; Cavalli, R.; Guiot, C.; D'Agata, F. Magnetic Iron Oxide Nanoparticles: Synthesis, Characterization and Functionalization for Biomedical Applications in the Central Nervous System. *Materials* **2019**, *12*, 465. [CrossRef]
35. Ouma, I.L.; Naidoo, E.B.; Ofomaja, A.E. Thermodynamic, kinetic and spectroscopic investigation of arsenite adsorption mechanism on pine cone-magnetite composite. *J. Environ. Chem. Eng.* **2018**, *6*, 5409–5419. [CrossRef]
36. Alemdar, A.; Sain, M. Crystallinity of natural polymers: A review. *Polym. Eng. Sci.* **2008**, *48*, 1–12.
37. Li, Z.; Yan, Y.; Wang, Y.; Zhang, Y.; Tang, Z.; Li, Y. A facile method to prepare cellulose nanocrystal reinforced graphene oxide nanocomposite with enhanced crystallinity and thermal conductivity. *Cellulose* **2020**, *27*, 4405–4418.
38. Li, Y.; Wang, Y.; Yan, Y.; Zhang, Y.; Tang, Z. Enhanced mechanical and thermal properties of silica nanoparticle reinforced cellulose nanocrystal bionanocompo-sites. *Cellulose* **2019**, *26*, 573–589.

39. Gül, H.; Yılmaz, N.; Karakaya, S. Effect of Iron Oxide Nanoparticles on Crystallinity, Mechanical Properties, and Thermal Stability of Cellulose Nanocomposites. *Macromol. Res.* **2018**, *26*, 1057–1065.
40. Marques, A.M.; Correia, M.L.; Branquinho, R. Structural and morphological characterization of cellulose nanocrystals and magnetic iron oxide nanoparticles composites: A combined approach of X-ray diffraction, atomic force and electron microscopy. *Appl. Surf. Sci.* **2020**, *506*, 144–153. [CrossRef]
41. Meda, R.S.; Jain, S.; Singh, S.; Verma, C.; Nandi, U.; Maji, P.K. Novel Lagenaria siceraria peel waste based cellulose nanocrystals: Isolation and rationalizing H-bonding interactions. *Ind. Crops Prod.* **2022**, *186*, 115197. [CrossRef]
42. Kupeta, A.J.K.; Naidoo, E.B.; Ofomaja, A.E. Chromate Ion Adsorption onto Nanostructured Mn–Fe Oxide Kinetics and Equilibrium Study. In *International Conference on Pure and Applied Chemistry*; Springer: Cham, Switzerland, 2018; pp. 269–282. [CrossRef]
43. Wang, X.; Guo, Y. The impact of trace metal cations and absorbed water on colour transition of turquoise. *R. Soc. Open Sci.* **2021**, *8*, 201110. [CrossRef] [PubMed]
44. Amiralian, N.; Annamalai, P.K.; Garvey, C.J.; Jiang, E.; Memmott, P.; Martin, D.J. High aspect ratio nanocellulose from an extremophile spinifex grass by controlled acid hydrolysis. *Cellulose* **2017**, *24*, 3753–3766. [CrossRef]
45. Candido, R.; Godoy, G.; Gonçalves, A.R. Characterization and application of cellulose acetate synthesized from sugarcane bagasse. *Carbohydr. Polym.* **2017**, *167*, 280–289. [CrossRef] [PubMed]
46. Yin, S.; Liu, J.; Kang, Y.; Lin, Y.; Li, D.; Shao, L. Interactions of nanomaterials with ion channels and related mechanisms. *J. Cereb. Blood Flow Metab.* **2019**, *176*, 3754–3774. [CrossRef] [PubMed]
47. Johar, N.; Ahmad, I.; Dufresne, A. Extraction, preparation and characterization of cellulose fibres and nanocrystals from rice husk. *Ind. Crop. Prod.* **2012**, *37*, 93–99. [CrossRef]
48. Kumar, A.; Negi, Y.S.; Choudhary, V.; Bhardwaj, N.K. Characterization of cellulose nanocrystals produced by acid-hydrolysis from sugarcane bagasse as agro-waste. *J. Mater. Phys. Chem.* **2014**, *2*, 1–8. [CrossRef]
49. Xu, P.; Han, X.; Wang, C.; Zhao, H.; Wang, J.; Wang, X.; Zhang, B. Synthesis of electromagnetic functionalized barium ferrite nanoparticles embedded in polypyrrole. *J. Phys. Chem. B* **2008**, *112*, 2775–2781. [CrossRef]
50. Wang, F.; Zhang, D.; Chen, M.; Yi, W.; Wang, L. Characteristics of corn stover components pyrolysis at low temperature based on detergent fibres. *Front. Bioeng. Biotechnol.* **2019**, *7*, 188. [CrossRef]
51. Chandra, C.S.J.; George, N.; Narayanankutty, S.K. Isolation and characterization of cellulose nanofibrils from arcanum husk fibre. *Carbohydr. Polym.* **2016**, *142*, 158–166. [CrossRef]
52. Al Aiti, M.; Jehnichen, D.; Fischer, D.; Brünig, H.; Heinrich, G. On the morphology and structure formation of carbon fibers from polymer precursor systems. *Prog. Mater. Sci.* **2018**, *98*, 477–551. [CrossRef]
53. Jeon, H.; Cho, H.; Lee, S.; Kim, K.; Kim, J.; Kim, H. Investigation of thermal properties of magnetite/cellulose nanocrystal/cellulose composite materials. *Polym. Test.* **2018**, *67*, 156–162.
54. Akhtar, J.; Sharma, S.; Jain, S.; Jain, N. Thermal stability of cellulose and cellulose nanocrystal reinforced with iron oxide nanoparticles. *Polymers* **2020**, *12*, 1822. [CrossRef]
55. Krishnamurthy, S.S.; Subbareddy, M.V.; Bandyopadhyay, A.K.; Ray, A.K. Synthesis and Characterization of Iron Oxide Nanoparticles by Hydrothermal Method. *Mater. Sci. Eng.* **2008**, *148*, 57–61. [CrossRef]
56. Zhou, Z.; Xu, Y.; Wang, Z.; Xiong, L.; Zhang, G.; Wang, X.; Cao, J. Synthesis and characterization of iron oxide nanoparticles by chemical precipitation method. *J. Magn. Magn. Mater.* **2011**, *323*, 1383–1388. [CrossRef]
57. Liu, Y.; Zhang, S.; Jiang, L.; Wu, Y.; Zhang, J.; Luo, X.; Ma, Y. Modification of cellulose-based materials with iron oxide nanoparticles. *Cellulose* **2016**, *23*, 1457–1468. [CrossRef]
58. Du, H.; Liu, W.; Zhang, M.; Si, C.; Zhang, X.; Li, B. Cellulose nanocrystals and cellulose nanofibrils based hydrogels for biomedical applications. *Carbohydr. Polym.* **2019**, *209*, 130–144. [CrossRef]